Section 5

Development of and studies with regional and convective-scale atmospheric models and ensembles.

Hurricane Analysis and Forecast System (HAFS) Stand-alone Regional (SAR) Model: Real-time Experiments for 2019 North Atlantic Hurricane Season

Jili Dong[1,2], Bin Liu[1,2], Zhan Zhang[1,2], Weiguo Wang[1,2], Lin Zhu[1,2], Chunxi Zhang[1,2], Keqin Wu[1,2], Andrew Hazelton[2,3], Xuejin Zhang[2], Avichal Mehra[2], and Vijay Tallapragada[2]

[1]IMSG at EMC/NCEP/NWS/NOAA, College Park, MD 20740 [2]EMC/NCEP/NWS/NOAA, College Park, MD 20740 [3]CIMAS/University of Miami, Miami, FL 33149

Email: Jili.Dong@noaa.gov

1. Introduction

The next generation hurricane forecast system Hurricane Analysis and Forecast System (HAFS) has been developed to accelerate improvements in tropical cyclone (TC) intensity and track forecasts within a unified global and regional modelling framework. HAFS utilizes the Finite Volume Cubed Sphere (FV3) based global-regional modelling system for TC prediction. The system can be applied in either a high resolution regional stand-alone regional model (HAFS v0.A or HAFS-SAR) or a uniform global model with a high resolution nest mode (HAFS v0.B or HAFS-global-nest). HAFS-SAR has been developed to cover the North Atlantic basin for hurricane forecasting (Fig. 1) and includes improved planetary boundary layer (PBL) and surface flux parameterization schemes designed specifically for TC predictions. The workflow for HAFS v0.A has also been developed to include preprocessing, post-processing, and a vortex tracker.

Both the HAFS-global-nest and HAFS-SAR were successfully implemented in real-time HFIP experiments for the 2019 North Atlantic hurricane season. The results are analyzed and compared with other regional and global models for further evaluation.

2. HAFS-SAR model

The FV3 based HAFS regional model has a single domain with the dimensions 2880 by 1920. The domain covers the North Atlantic basin with a horizontal resolution of 3 km. HAFS-SAR has 64 vertical levels on the sigma-pressure hybrid coordinate, with the lowest model level at about 25m above the surface and the top level at 0.2 hPa. Initial and boundary conditions are interpolated from the Global Forecast System (GFS) (~13 km) onto the HAFS SAR domain. Lateral boundary conditions (LBCs) are provided every 3 hours from the same GFS forecasts.

Physics parameterizations in HAFS SAR include the EDMF PBL scheme and GFS surface fluxes scheme, which are further modified with a formula from HWRF, and the GFDL microphysics scheme with 6 category hydrometeors. HAFS-SAR also uses the same GFS land surface scheme and RRTMG longwave and shortwave parameterizations. Cumulus convection is turned off at the convective scale resolution ~ 3 km. SST is from the GFS Near-Sea-Surface Temperature (NSST) scheme which predicts the vertical profile of ocean temperature between the surface and a reference level.

3. 2019 real-time experiments

2019 HAFS SAR real-time experiments for the North Atlantic hurricane season started on July 13, 2019 and ended on November 1, 2019. The experiments were performed on the NOAA RDHPCS Jet supercomputer and covered 18 storms with a total of 269 cycles. The track forecast error of HAFS-SAR is smaller than the GFS and the two regional hurricane models HWRF and HMON at almost all forecast lead times (Fig. 2a). Track forecast skill is improved about 20% by HAFS-SAR with respect to HWRF throughout the 5 days of forecasts (Fig. 2b). The cross-track component contributes more to the track forecast improvement than the along-track component. The initial intensity error of HAFS-SAR is comparable to that of GFS, due to the lack of inner core data assimilation. Intensity error is reduced within the first 6 hours of spin-up and then grows until 72 hours (Fig. 2c). The intensity error of HAFS-SAR at day 5 is lower than other models presented here.

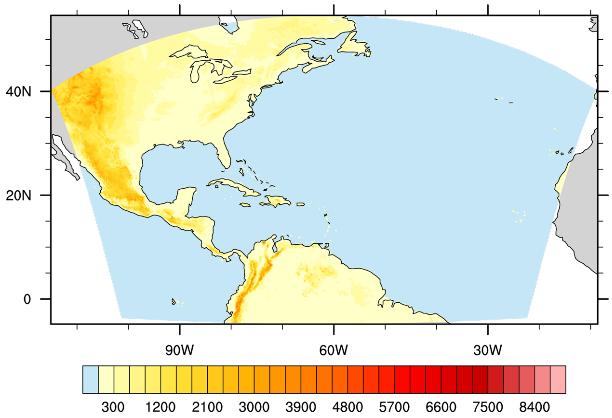

The intensity bias is generally negative before day 5, suggesting an underprediction of TC intensity from HAFS-SAR, along with other models (Fig. 2d). The intensity forecasts of weak storms have better performance than strong storms when stratified with 50-kt thresholds.

Fig. 1: HAFS-SAR domain for 2019 north Atlantic hurricane season.

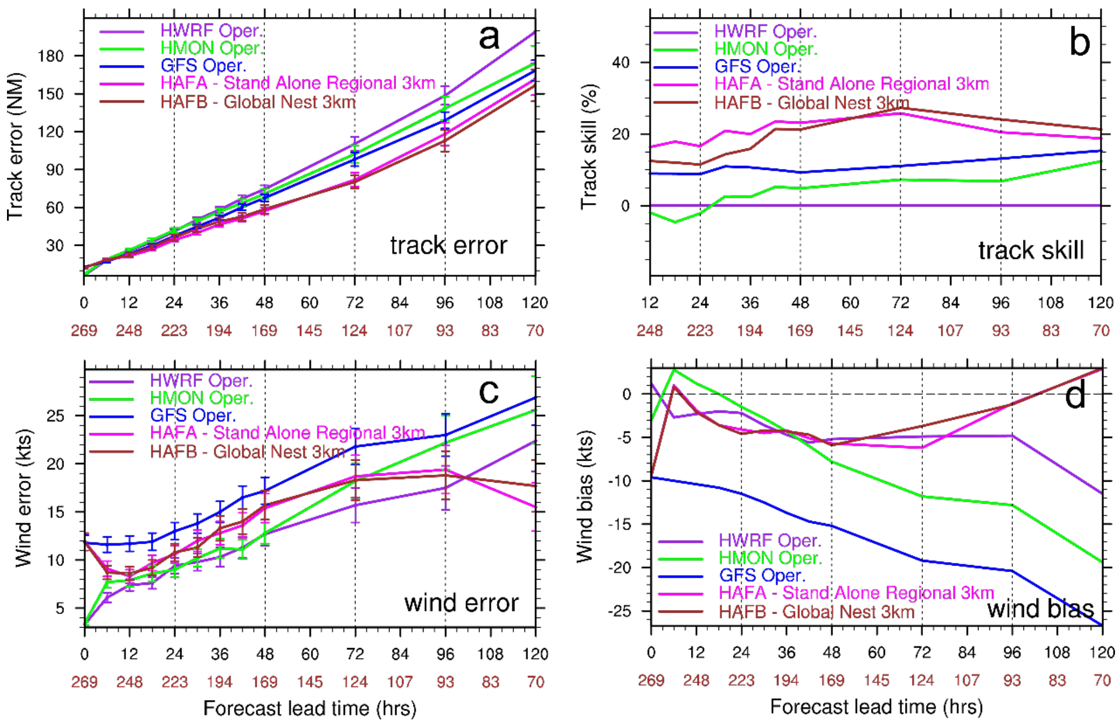

Fig. 2: (a) Track error statistics for HAFS-SAR, HAFS-global-nest, operational GFS, HWRF and HMON; (b) Track skill; (c) Intensity error statistics (wind); (d) Intensity bias statistics (wind).

4. Summary

For the 2019 North Atlantic hurricane season, the FV3-based HAFS-SAR showed great potential to improve TC forecasts, particularly the track forecasts. The improvement for high-impact storms (e.g., Barry and Dorian) is also very encouraging. Inner core data assimilation being developed for HAFS is expected to further improve the intensity forecasts.

Numerical simulation of the seasonal precipitation amount over the Himalayan mountain region using the JMA-NHM

Akihiro Hashimoto[1], Masashi Niwano[1], Hatsuki Fujinami[2], Akiko Sakai[3], and Koji Fujita[3]

[1]*Meteorological Research Institute, Japan Meteorological Agency, Tsukuba, Japan*
[2] *Institute for Space-Earth Environmental Research, Nagoya University, Nagoya, Japan*
[3]*Graduate School of Environmental Studies, Nagoya University, Nagoya, Japan*

1. Introduction

In the last several decades, there has been a rapid retreat of the Himalayan glaciers. This has raised concerns regarding the effect of glacial retreat on river flow and water resources in South Asia which is experiencing rapid population growth. Precipitation over the Himalayan mountain region is a strong factor that affects the mass balance of the glaciers. For reliable prediction of the mass retreat of glaciers, it is necessary to understand the spatiotemporal distribution of precipitation and its impact on glacier mass balance and dynamics of water discharge. Satellite earth observation projects, such as Tropical Rainfall Measuring Mission (TRMM) and Global Precipitation Measurement (GPM), provide valuable data that enable statistical evaluation of the spatial distribution of precipitation covering a broad area, including the Himalayas. However, it is difficult to apply such data for detailed evaluation of seasonal changes to precipitation quantity and patterns due to intermittent spaceborne measurements. A complementary solution to address this issue is to use a numerical weather prediction (NWP) model. In this study, we plan to evaluate the glacier accumulation in the Himalayan mountain region using an NWP model with fine grid spacing. This report presents the results of preliminary simulations in terms of the sensitivity of simulated precipitation to grid spacing.

2. Numerical prediction system

The numerical prediction system was established based on the Japan Meteorological Agency's Non-Hydrostatic Model (JMA-NHM; Saito et al., 2006). The model was configured in the same manner as that previously used for the operational weather forecast in Japan, with the exception of the following: (i) in this study, a double-moment bulk parameterization scheme, predicting the mixing ratio and number concentration, was applied to all the three types of solid hydrometeors (cloud ice, snow and graupel), whereas this scheme was applied only to cloud ice in the original configuration; (ii) the ice-saturation adjustment scheme (Tao et al., 1989) was switched off to avoid the unrealistic formation of ice clouds in the upper troposphere.

Numerical predictions were conducted once a day from 1 June, 2018, to 31 May, 2019. For each prediction, the simulation was first conducted with a 5-km horizontal resolution (5km-NHM). The computational domain spans 2000 km × 2000 km wide (Fig. 1). Next, a convection permitting simulation with a 1 km horizontal resolution (1km-NHM) was conducted without cumulus parameterization in the domain (800 × 800 grid cells) embedded within the 5km-NHM (Fig. 1). Both domains were centered at Kathmandu, Nepal. The Lambert conformal conic projection was adopted, using 30.00 and 60.00°N for the

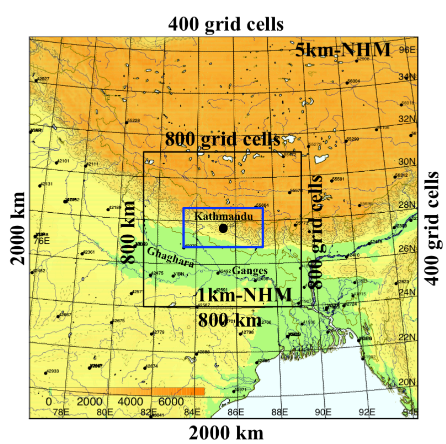

Fig. 1. Computational domains for weather prediction simulations with the 5km- and 1km-NHMs. The blue box shows the sampling area analyzed for seasonal changes in altitudinal variations of accumulated precipitation.

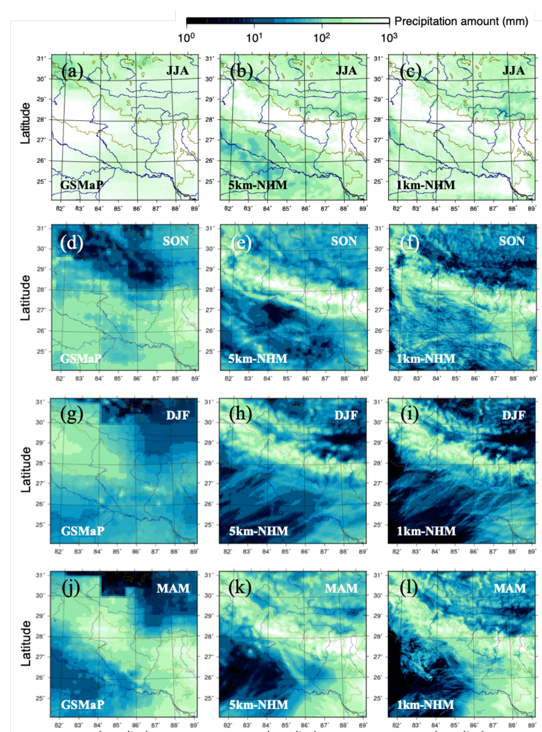

Fig. 2. Distributions of seasonal accumulated precipitation amount within the area corresponding to the domain of the 1km-NHM based on the observations with GSMaP (a, d, g, j), and the simulations with the 5km-NHM (b, e, h, k) and 1km-NHM (c, f, i, l). JJA, SON, DJF, and MAM indicate three-month periods from June, September, December 2018, and March 2019, respectively.

Corresponding author: Akihiro Hashimoto, Meteorological Research Institute, 1-1 Nagamine, Tsukuba, 305-0052, Japan. E-mail: ahashimo@mri-jma.go.jp

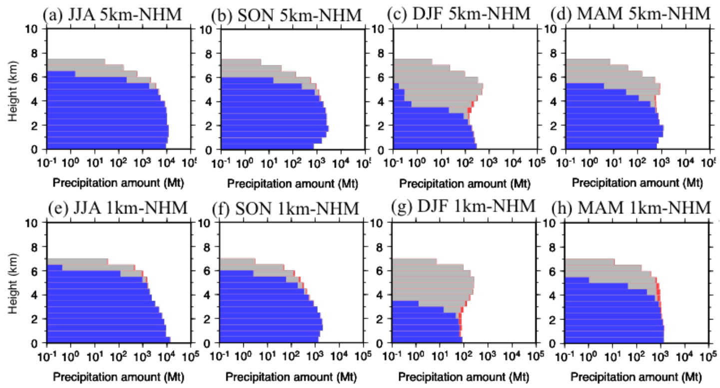

Fig. 3. Altitudinal variations of the three-month accumulated precipitation amount in the (a, e) JJA, (b, f) SON, (c, g) DJF, and (d, h) MAM periods from the simulations using the 5km-NHM (a, b, c, d) and 1km-NHM (e, f, g, h). Blue, grey, and red indicate different precipitation types: rain, snow, and graupel, respectively. The height interval is 500 m.

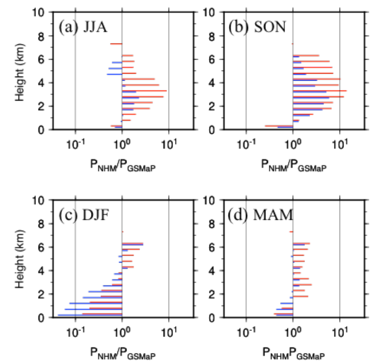

Fig. 4. Altitudinal variations of the ratio of the accumulated precipitation amount from simulations to the accumulated precipitation from GSMaP. The red and blue bars show the results generated by the 5km- and 1km-NHMs, respectively.

first and second standard latitudes, respectively, and 85.00°E for the standard longitude in both domains. The top height of the domain was 22 km, and there were 50 layers in the vertical direction, increasing from 40 m thick at the surface to 886 m at the top based on a terrain-following coordinate system.

The integration time for the 5km-NHM was 48 h, with a timestep of 8 s. The initial and boundary conditions were obtained from the JMA's operational global forecast. The simulation commenced at 1200 coordinated universal time (UTC), corresponding to a forecast time (FT) of 6 h in the JMA's operational global forecast beginning at 0600 UTC. The boundary conditions were provided every 6 h. For the 1km-NHM, the simulation commenced at a FT of 18 h in the 5km-NHM simulation, and the integration time was 27 h with an 8 s timestep. The initial and boundary conditions were obtained from the 5km-NHM.

3. Simulation results

Figure 2 illustrates the distributions of seasonal accumulated precipitation amount provided by the Global Satellite Mapping of Precipitation (GSMaP), and that simulated using the 5km- and 1km-NHMs. Whilst the GSMaP product has a bias compared to rain gauge measurements, in the present context, we considered it representative of observed data for comparison with the simulation results in this report. In summer (June-August; JJA), the GSMaP shows that the precipitation area covers the low land surrounding the Ghaghara and Ganges rivers, the high altitude mountain area, and the Tibetan plateau (Fig. 2a). The 5km-NHM underestimated the precipitation in the low land area (Fig. 2b), whilst the 1km-NHM provided a better prediction of this distribution in the low land area. (Fig. 2c). The precipitation decreases in autumn (September-November; SON), particularly in the Tibetan plateau (Fig. 2d). The 5km-NHM showed negative bias toward the low land area, and a positive bias toward the high mountain area and Tibetan plateau (Fig. 2e), compared with GSMaP. The 1km-NHM predicted greater precipitation in the low land than in the Tibetan plateau (Fig. 2f), consistent with results from GSMaP (Fig. 2d). Although precipitation in the high mountain area was overestimated, the 1km-NHM generally provided more accurate results than the 5km-NHM. However, the superiority of the 1km-NHM over the 5km-NHM was unclear in winter (December–February; DJF) and spring (March–May; MAM).

Figures 3 shows the altitudinal variations of precipitation amount within the blue box in Fig. 1 for different seasons simulated with the 5km- and 1km-NHM. In summer (JJA) and autumn (SON), the 1km-NHM predicted greater precipitation in the low land area at altitudes less than 500 m (Figs. 3e and 3f), compared with the 5km-NHM (Figs. 3a and 3b). Beyond 2 km above sea level (a.s.l.), the predicted precipitation by the 1km-NHM was less than predicted by the 5km-NHM. These features are consistent with the results in Fig. 2, where there is greater and reduced precipitation in low and high land areas, respectively, in the 1km-NHM than in the 5km-NHM. Figure 4 presents the ratio of the accumulated precipitation amount from the 5km-NHM (red bar) or 1km-NHM (blue bar) simulations to the GSMaP. The results of the 1km-NHM show better agreement with GSMaP than the results from the 5km-NHM in summer and autumn (Figs. 4a and 4b, respectively). This is consistent with the features presented in Fig. 3. In winter (Fig. 4c), the 1km-NHM underestimates precipitation at altitudes lower than 3 km. In spring (Fig. 4d), the 1km-NHM showed better results at the altitudes higher than 2 km.

The simulation results demonstrate the effectiveness of adopting a 1 km convection permitting grid spacing for regional simulation of precipitation in the Himalayan mountain region, particularly, for summer and autumn. However, rain-gauge-based validation is necessary to ensure the improved performance of the 1 km grid spacing.

Acknowledgements

This study is partly supported by the Joint Research Program with Swiss National Science Foundation "High elevation precipitation in High Mountain Asia" of Japan Society for the Promotion of Science (JPSP), and the Ministry of the Environment of Japan through the Experimental Research Fund for Global Environmental Research Coordination System.

References

Saito, K., T. Fujita, Y. Yamada, J. Ishida, Y. Kumagai, K. Aranami, S. Ohmori, R. Nagasawa, S. Kumagai, C. Muroi, T. Kato, H. Eito, and Y. Yamazaki, 2006: The operational JMA nonhydrostatic mesoscale model. *Mon. Wea. Rev.*, **134**, 1266–1298.

Tao, W.-K., J. Simpson, and M. McCumber, 1989: An ice- water saturation adjustment. *Mon. Wea. Rev.*, **117**, 231–235.

Numerical simulations of the cloud and precipitation processes during the heavy rainfall events of early July 2017 and 2018 in Japan

Akihiro Hashimoto and Syugo Hayashi

Meteorological Research Institute, Japan Meteorological Agency, Tsukuba, Japan

1. Introduction

From July 5 to 6, 2017, stationary convective systems brought heavy rainfall to northern Kyushu, where a total rainfall amount of more than 300 mm was recorded at several observation sites, with 586 mm being recorded at Asakura in Fukuoka Prefecture. This rainfall event caused river floods and landslides, leading to serious damage to houses, transportation networks, and public utilities such as electricity and water. In addition, there were 40 deaths and 2 people went missing (Cabinet Office Japan, 2018). A year later, from late June to early July 2018, a wide area of western Japan was struck by record heavy rainfall. The total rainfall recorded during the period June 28 to July 8 was more than 500 mm in many places: in particular, 1852 mm was recorded at Yanase in Kochi Prefecture. This event also caused enormous damage, as well as 237 deaths and more than 400 injuries. Eight persons were recorded as missing (Cabinet Office Japan, 2019).

These heavy rainfall events were investigated from a synoptic-scale to mesoscale perspective by several studies. Based on the results of numerical simulations, this report presents preliminary results on the microphysical characteristics of these two events.

2. Numerical simulations

A numerical simulation system was established based on the Japan Meteorological Agency's nonhydrostatic model (JMA-NHM, Saito *et al*., 2006) using the option of a double-moment bulk cloud microphysics scheme to predict both the mixing ratio and concentration of particles for all hydrometeor classes (i.e., cloud water, rain, cloud ice, snow, and graupel).

The numerical simulations were successively conducted once a day, shifting the initial time in 24-hour steps from July 3 to 6, 2017 and from July 4 to 7, 2018. Each simulation was first performed at a horizontal resolution of 5 km (5km-NHM) over a 2750 km × 3000 km wide domain as shown in Fig. 1. Following this, simulations with a 1-km horizontal resolution were performed and were named 1km-NHM-KYS and 1km-NHM-CGK for the 2017 and 2018 events, respectively (Fig. 1).

In the case of 5km-NHM, the top height of the model domain was 22 km. The vertical grid spacing ranged from 40 m at the surface to 723 m at the top of the domain. Sixty vertical layers in a terrain-following coordinate system were employed. The integration time was 45 hours, with a time-step of 15 s. Computations of the radiative processes were performed every 15 minutes at a horizontal grid spacing of 10 km. The initial and boundary conditions were obtained from the JMA's mesoscale analysis data (MANAL). The initial time was set to 1500 JST (UTC + 9) for each day. Boundary conditions were provided with steps of every 3 hours.

Corresponding author: Akihiro Hashimoto, Meteorological Research Institute, 1-1 Nagamine, Tsukuba, 305-0052, Japan. E-mail: ahashimo@mri-jma.go.jp

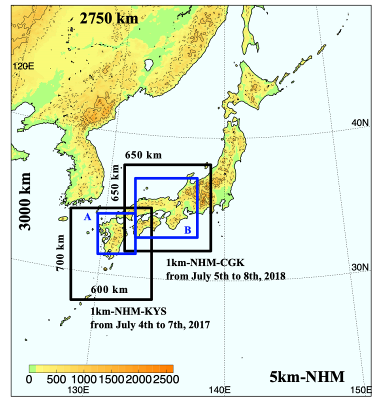

Fig. 1. Computational domains for the numerical simulations: 5km-NHM, 1km-NHM-KYS, and 1km-NHM-CGK.

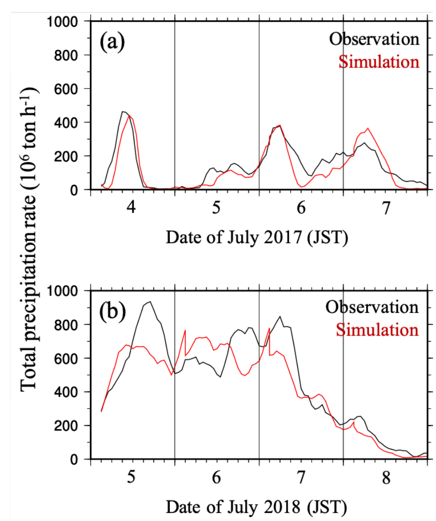

Fig. 2. Time-series of the total precipitation rate for the heavy rainfall events in (a) 2017 and (b) 2018, which were evaluated for the areas within the blue boxes A and B, respectively, shown in Fig. 1. The black and red lines denote the observations and simulations, respectively.

The vertical grid arrangement in the 1km-NHM-KYS was the same as in the 5km-NHM, and the domain size was 600 km × 700 km (Fig. 1). The integration time used was 30 hours with a timestep of 4 s. Computations of the radiative process were performed every 15 minutes at a horizontal grid spacing of 2 km, and the initial and boundary conditions were obtained from the 5km-NHM simulation. The same configuration was adopted for the 1km-NHM-CGK, except that the domain size was 550 km × 600 km and the simulation was centered on Chugoku district (Fig. 1). The initial time for the 1km-NHM-KYS and CGK simulations was 12 hours later than that of the 5km-NHM.

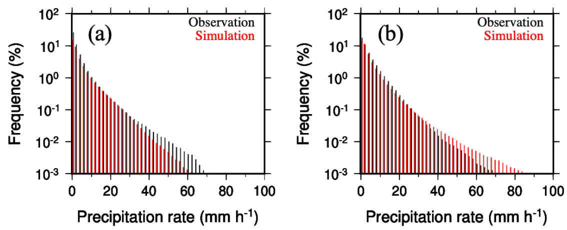

Fig. 3. Appearance frequency for the total precipitation rate for the heavy rainfall events in (a) 2017 and (b) 2018, as evaluated for the areas within the blue boxes A and B, respectively, shown in Fig. 1. The black and red bars denote the observations and simulations, respectively.

3. Results

To validate the results of simulation, we first compared the simulated precipitation intensity with the observations; the Radar/Raingauge-Analyzed Precipitation product provided by the JMA. Figure 2a shows the time-series of the total precipitation rate evaluated for area A in Fig. 1 for the heavy rainfall event in 2017. The rainfall in July 4 was that associated with the typhoon Nanmadol. A disastrous rainfall event occurred in Fukuoka Prefecture occurred on July 5 and 6. The simulated total precipitation rate was in good agreement with the observations throughout the period of the simulation. For the 2018 event as shown in Fig. 2b, the simulation slightly underestimated the precipitation rate. Figure 3 shows the appearance frequency for the total precipitation rate. Rainfall with an intensity of about 20 mm h^{-1} was well represented by the simulation of the 2017 event, whereas lighter and heavier rainfall was underestimated. In the case of the 2018 event, the appearance frequency of the rainfall with an intensity of less than 25 mm h^{-1} was underestimated, whereas rainfall with an intensity greater than this was overestimated by the simulations.

Hamada and Takayabu (2018) stated that the extreme rainfall events in midsummer in Japan are not necessarily accompanied by extreme convection or lightning activity. Figure 4 shows a time-series of the flash rate observed by the Lightning Detection Network system (LIDEN) of the JMA. The flash rate during the 2018 event was one or two orders of magnitude lower than during the 2017 event. This is notable considering that the total precipitation rate (Fig. 2) recorded during the 2018 event was larger than in the 2017 event throughout most of the simulation period. The simulated updraft velocity was larger and the peak height was higher during the 2017 event than in the 2018 event. Figure 5 shows the appearance frequency of the mixing ratios of hydrometeors. In the 2017 event, supercooled liquid water and graupel were found to prevail throughout the troposphere to a much greater extent than in the 2018 event. Generally speaking, lightning activity is closely related to the existence of graupel in a cloud. The simulated results indicate that the difference in flash rate between the two events was produced by the microphysical differences shown in Fig. 5.

Figure 4 also shows the simulated graupel-dominated volume (the sum of all the grid volumes in which the mixing ratio for graupel is the largest among the modeled hydrometeors). In both events, the temporal changes in the simulated graupel-dominated volume roughly correspond to the changes in the observed flash rate, which indicates the potential of constructing a regional weather prediction model that can be used to make dynamical predictions of the flash rate.

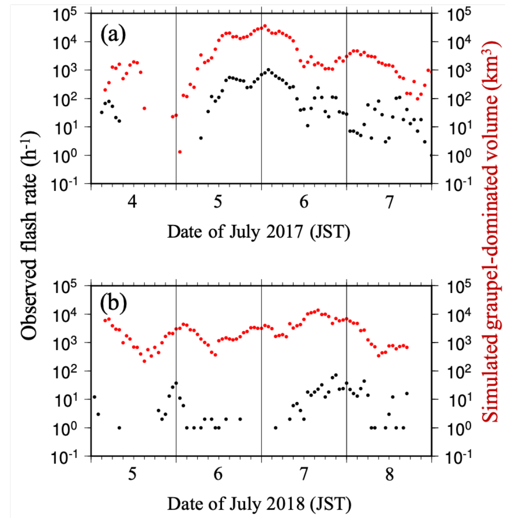

Fig. 4. Simulated graupel-dominated volume (red dots) and observed flash rate (the number of cloud-to-ground lightning strikes per hour: black dots) for the heavy rainfall events in (a) 2017 and (b) 2018, as evaluated for the areas within the blue boxes A and B, respectively, shown in Fig. 1.

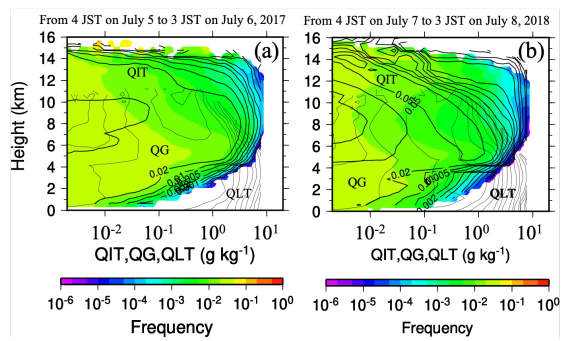

Fig. 5. Appearance frequency for the mixing ratio of total solid water (QIT: black contours), graupel (QG: color shading), and total liquid water (QLT: gray contours) for the (a) 2017 and (b) 2018 events.

Acknowledgements

This work was performed under the Fundamental Technology Research of the Meteorological Research Institute, and partly supported by the JSPS KAKENHI Grant Number 20H04196.

References

Cabinet Office Japan, 2018: *White paper on disaster management in Japan 2018.* 129pp. (http://www.bousai.go.jp/kaigirep/hakusho/pdf/H30_hakusho_english.pdf, accessed 28 April 2020)

Cabinet Office Japan, 2019: *White paper on disaster management in Japan 2019.* 140pp. (http://www.bousai.go.jp/kaigirep/hakusho/pdf/R1_hakusho_english.pdf, accessed 28 April 2020)

Hamada, A. and Y. Takayabu, 2018: Large-Scale Environmental Conditions Related to Midsummer Extreme Rainfall Events around Japan in the TRMM Region. *J. Climate*, 31, 6933-6945, doi:10.1175/JCLI-D-17-0632.1.

Saito, K., T. Fujita, Y. Yamada, J. Ishida, Y. Kumagai, K. Aranami, S. Ohmori, R. Nagasawa, S. Kumagai, C. Muroi, T. Kato, H. Eito, and Y. Yamazaki, 2006: The operational JMA nonhydrostatic mesoscale model. *Mon. Wea. Rev.*, **134**, 1266–1298.

Super-Cyclone Amphan (2020) : Global versus Regional Ensemble Prediction

Manpreet Kaur[a], A. K. Sahai[a,*], R. Phani[a], and Susmitha Joseph[a]

[a]Indian Institute of Tropical Meteorology, Ministry of Earth Sciences, India; [*]*E-mail: sahai@tropmet.res.in*

The India meteorological department extended range forecast (IMDERF) from 13 May initial condition (IC) evinced 60-80% genesis probability of an approaching storm. However, this forecast lacked in storm intensity and trajectory. Considering the system indication in IMDERF, this ensemble forecast is downscaled using one-way nested Weather Research and Forecasting (WRF) model. The short comparison of the global and regional ensemble predictions from 13 May 2020 IC is presented here.

The advanced scientific and computing resources equipped the forecasters with a range of prediction tools across spatial and temporal scales of weather phenomena. Nevertheless, the rare and unforeseen hazards intermittently put these tools on the test. One such event was the Bay of Bengal (BOB) super cyclone Amphan. Amid the ongoing global pandemic, the first cyclone of 2020 pre-monsoon season in the North Indian Ocean caused havoc in the Eastern Indian states as well as Bangladesh. This cataclysmic storm was one of the strongest occurring in the BOB basin over the past 20 years. The system appeared as low in southwest BOB on 13 May and later organized into cyclonic storm Amphan on 16 May. Amphan rapidly intensified from severe to an extremely severe cyclone on subsequent days, finally amplifying to a super cyclone on 18 May. It slightly weakened under unfavorable shear conditions, still entered West Bengal - Bangladesh coast with high ($45 m.s^{-1}$) wind-gust (IMD, 2020a, 2020b).

Methodology

Global Ensemble System. The operational extended range forecast (IMDERF) is an ensemble of 16 members based on two resolution (T382 and T126) variations of Climate Forecast System and its atmospheric model Global Forecast System(GFS). IMDERF is being generated once every week since 2016.

Regional Ensemble System. The WRF runs are performed with a specified regional domain (25°S-55°N, 30°E-128°E) to downscale all IMDERF ensemble members (M_i) independently. To control systematic error amplification, the global model climatology ($\overline{M}$) is corrected with Climate System Forecasts Reanalysis climatology ($\overline{R}$) beforehand.

$$M_i^{bc} = (M_i - \overline{M}) + \overline{R} \qquad [1]$$

The above correction is applied to all input meteorological variables, the horizontal resolution is targeted at 9km for regional ensemble run. This bias-corrected downscaled ensemble is termed as BC-D-ERF hereafter. Further details can be found in (Kaur et al., 2020) and references therein.

Results

The observed maximum rainfall (Figure 1a) pattern during the cyclonic storm Amphan (during the event) was extended

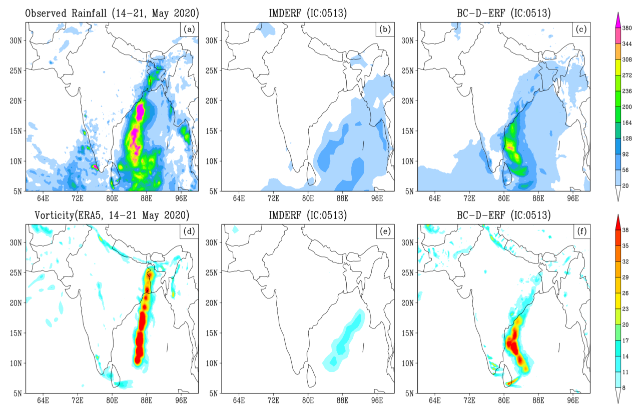

Fig. 1. Evolution of (a-c)maximum Rainfall (mm.day^{-1}) and (d-f) 850hPa vorticity(x10^{-5} S^{-1}) for observation, IMDERF, and BC-D-ERF respectively.

from south-west BOB to head Bay, over the North-Eastern parts of India and Bangladesh. The highest recorded rainfall associated with the event was more than 380 mm.day^{-1}. IMDERF ensemble mean rainfall (Figure 1b) has an eastward positional shift towards Myanmar, and the predicted magnitude is less than 92 mm.day^{-1}. The BC-D-ERF (Figure 1c) also shows location error, but more close to observed distribution than IMDERF. It is evident from the figure that BC-D-ERF predicted rainfall intensity is significantly improved.

Similar inferences can be made from vorticity plots compared with ERA5 reanalysis (Figure 1d), both IMDERF (Figure 1e) and BC-D-ERF (Figure 1f) failed to capture the storm track. However, BC-D-ERF reproduced the temporal evolution of storm intensity to a good extent.

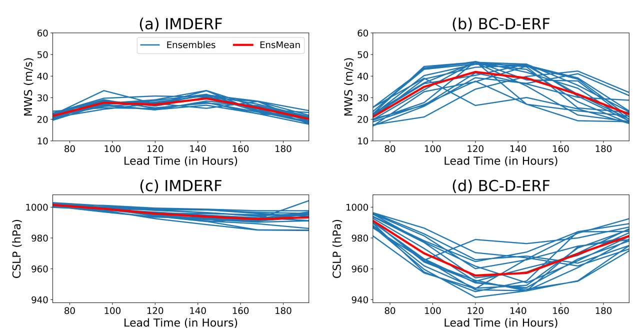

Fig. 2. 10m wind speed (MWS) and sea level pressure(CSLP) predicted by IMDERF(a & c) and BC-D-ERF (b & d)

It is worth mentioning here that IMD reported wind-gust of 155-165 kmph (43-45 m.s^{-1}) during the landfall of the cyclone Amphan. For further insights into the predicted surface winds, the system accompanying maximum 10m wind speed and minimum sea-level pressure predicted by IMDERF and BC-D-ERF are compared in Figure 2. IMDERF ensemble substantially underestimates the wind-speed (Figure 2a) as well as CSLP (Figure 2c), whereas the BC-D-ERF ensemble enacts MWS(Figure 2b) and CSLP(Figure 2d) reasonably well. It has predicted intensification of the system on 18 May (at lead 120hours), followed by a drop in the storm strength similar to the one documented by IMD. The BC-D-ERF ensemble has a larger spread promising better probabilistic skill than IMDERF.

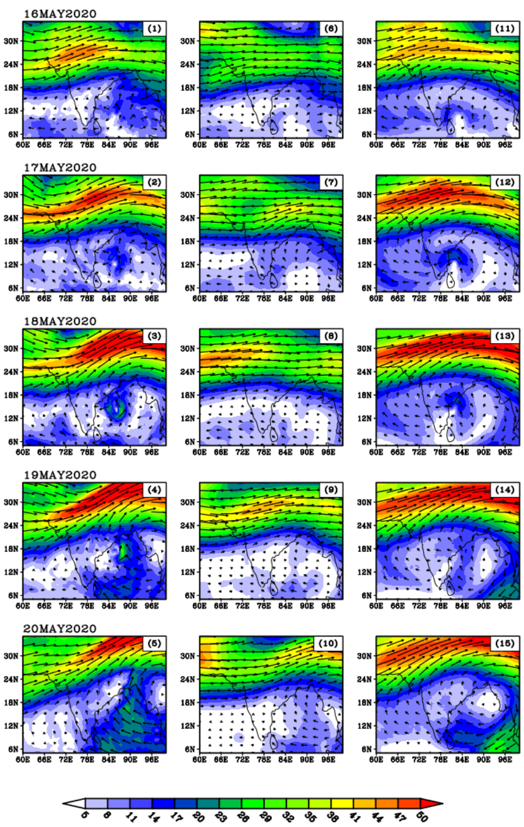

Fig. 3. 200hPa wind(m.s^{-1}) for ERA5(1-5), IMDERF(6-10) and BC-D-ERF(11-15) from 16-20 May

As inferred from Figure 1, the cyclonic system predicted by BC-D-ERF moved in the proximity of the east coast of India, and it weakened at lower latitudes than the observation. For better understanding, 200hPa wind from ERA5, IMDERF and BC-D-ERF are analyzed in Figure 3. ERA5 (Figure 3(1-5)) shows the cyclonic circulation associated with the system in BOB (17-19 May), and its outward flow interaction with strong anti-cyclonic circulation in the subtropical jet stream. The 200hPa wind in IMDERF(Figure 3(6-10)) is comparatively weaker with the dominant westerly component. On the other hand, BC-D-ERF (Figure 3(11-15)) simulated upper-level winds are stronger and have broader and upward shifted circulation maxima. Consequently, the system interaction with large scale flow, and hence trajectory is impacted. Since the large scale boundary conditions are crucial for downscaling, the upper-level circulation bias in BC-D-ERF could have probable origination from driving IMDERF fields. The other possible cause could be the regional model physics. An additional investigation is planned shortly.

Conclusions

Despite the strong genesis signal, the intensity and track forecast of the super cyclonic storm Amphan is mostly underestimated by the global ensemble prediction system IMDERF. The regional ensemble prediction (BC-D-ERF) generated by downscaling IMDERF rectified the storm forecast. BC-D-ERF imitated the temporal evolution of observed super cyclonic storm exceptionally well. The bias in upper-level wind led to a slightly imprecise system trajectory by BC-D-ERF, which can be refined with further understanding. In short, the regional ensemble has the potential for spatial-temporal improvement over the global ensemble in a 7day advance forecast.

ACKNOWLEDGMENTS. The Ministry of Earth Sciences, Govt. of India, fully funds research at the Indian Institute of Tropical Meteorology (IITM). The authors duly acknowledge Dr. D. R. Pattanaik from IMD, ERPAS group, and HPCS facility at IITM.

References

IMD. (2020a). A preliminary report on nwp model forecasts performance for super cyclone amphan. *Numerical Weather Prediction Division, India Meteorological Department Ministry of Earth Sciences (MoES), New Delhi*, 1–53.

IMD. (2020b). Press release for cyclone amphan. *India Meteorological Department Ministry of Earth Sciences (MoES), New Delhi*. Retrieved from https://mausam.imd.gov.in/imd_latest/contents/press_release.php

Kaur, M, Krishna, RPM, Joseph, S, et al . Dynamical downscaling of a multimodel ensemble prediction system: Application to tropical cyclones. Atmos Sci Lett. 2020; 1– 11. https://doi.org/10.1002/asl.971

Convection-permitting scale simulations reduce precipitation bias over North America

Jiali Wang[1], Rao Kotamarthi[1], Won Chang[2]

[1]Environmental Science Division, Argonne National Laboratory, Lemont, Illinois, USA
[2]Department of Mathematical Sciences, University of Cincinnati, Cincinnati, OH
Email: vrkotamarthi@anl.gov

Motivation

Deep convection is a key process in climate systems and the main source of precipitation, which is a vital component of the water cycle. Precipitation intensity is increasing across the Contiguous United States (CONUS) (Fig 1). This increase is robust — it is seen in observation data, model simulation outputs at convective parameterized (Chang et al. 2016) and convective permitting simulations (Chen et al. 2020); it is also seen in both summer and winter. In order to represent the water cycle in the state-of-the-art earth system models (ESMs), the deep convection has to be parameterized due to the coarse grid spacing of the ESMs. However, the sub-grid deep convection parameterization is a major source of uncertainty and model bias. In addition, coarse grid spacing is not able to capture fine-scale features of topography and results in underestimation of rainfall and snowfall over mountain regions. When the grid spacing goes to 4 km or less, the ESMs can solve the convection explicitly, so model bias and uncertainty in the water cycle can be significantly reduced, and the predictability of hydrological extremes can be improved. We refer to this scale of simulation as convection-permitting scale (C-P hereafter). We have conducted short-term 4km simulations over contiguous United States (CONUS) and found that, compared to our previously generated 12km simulations, the C-P simulation significantly reduced the bias in precipitation size and intensity, diurnal variations, as well as snowfall and snowpack.

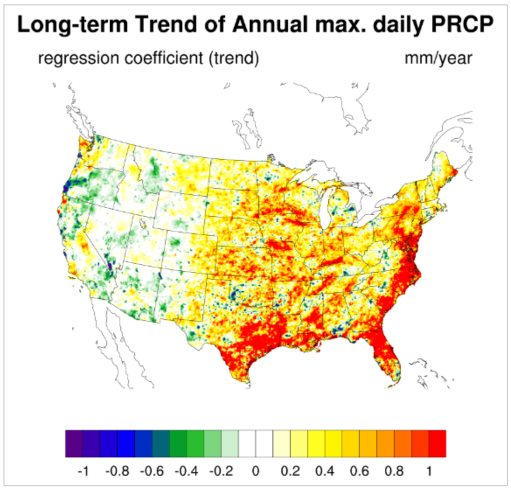

Figure 1. Long-term trend of annual maximum precipitation intensity based on 37 year of data from 1981 to 2017. The data is an observation-based gridded dataset on spatial resolution of 4km, called PRISM.

Model description: We conducted a suite of model runs at 4km horizontal resolution (C-P) using the Weather Research and Forecasting Model (WRF-ARW) version 3.3, with National Centers for Environmental Prediction Reanalysis II (NCEP) reanalysis for boundary and initial conditions. Simulation domains span most of North America, and the results shown here are for summer, 2005, June-August. The physics parameterizations used are WSM6 (WRF single-moment 6-class) microphysics (Hong and Lim 2006); Spectral nudging is applied above 850 hPa to wavelengths around 1200 km, with a nudging coefficient of $3\times10^{-5}s^{-1}$. We compare these 4km runs with the same setup but 12km with Grell–Devenyi convective scheme (GD) (Grell and Dévényi 2002) and Kain–Fritsch convective scheme (Kain 2004).

Results: The table below decomposed factors explaining precipitation bias for the model cases at 12km using GD and KF convective schemes, expressed as % anomaly vs stage IV (a gridded observation dataset). Precipitation distributions in both 12km simulations using GD (*2nd* column in the Table) and KF (*3rd* column in the Table) convective schemes are dominated by low-intensity and large-size rainstorm. The bias averaged over entire CONUS (compared with Stage IV observations) are 13% and 21% lower in intensity; and 150% and 220% higher in size. The explicit-convection 4 km reduces the wet bias in amount, and has a stronger mean intensity as well as a more accurate rainstorm size. While the model bias at monthly scale are similar between 12km and 4km resolution, the 4km capture better the smaller scale features, such as single severe storms (Fig. 2a) as well as diurnal variation (Fig. 2b), which is very important to describe the precipitation pattern in US, especially in warm season. Compare to observation data averaged over entire CONUS, all the models capture the diurnal cycle with peak in afternoon or evening, but 12km simulations generate too large and too regular peaks; and they also show an earlier minimum in the midnight. Specifically, over central great plains, all 12km simulations show early morning peaks while the observed peak is in late evening (not shown here). The 4km reduces the wet bias during the afternoon peak averaged over entire CONUS and is able to capture the diurnal curves over central great plains (not shown here).

Storm property	12km, GD	12km, KF	4km, C-P
Amount	58	68	29
Intensity	-13	-21	30
Size	150	220	33
Duration	-9	-4.6	-0.01
Num. of storms	-19	-42	-20

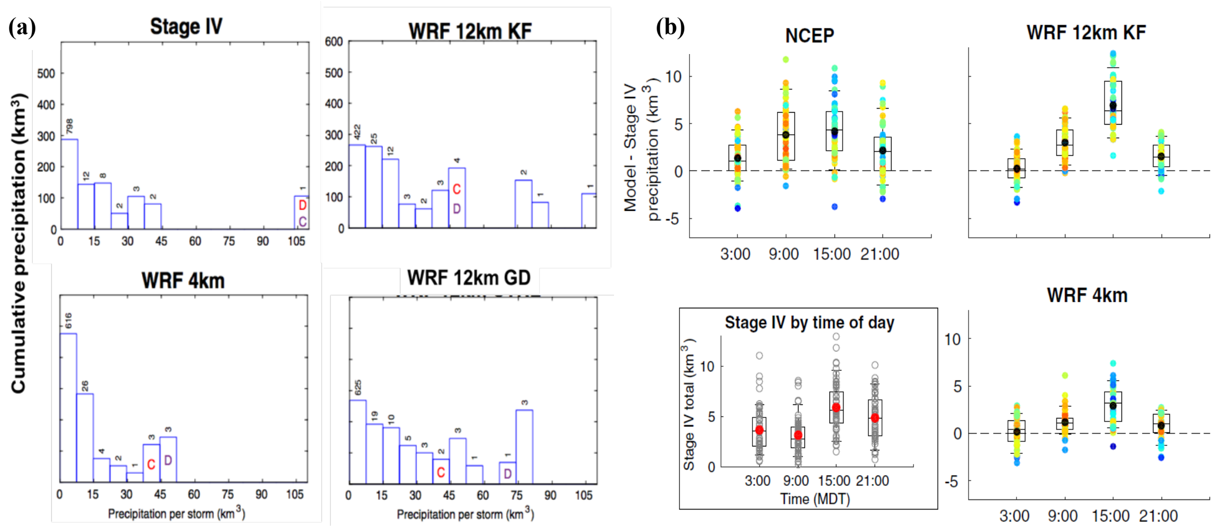

Figure 2 (a) Event-based precipitation distributions classed by individual storm precipitation amount. Numbers above each bar give the number of individual storms in each size bin. Labels 'C' or 'D' on a bin indicate the largest storm identified as part of Hurricanes Cindy or Dennis. (b) Box-Whisker plots of bias in diurnal cycle: absolute bias in domain-aggregated precipitation by time of day (mountain daylight time) for all model runs and for comparison, diurnal cycle in Stage IV observed precipitation. X-axis labels mark center of 6-h time intervals. and 9th and 91st percentiles of each distribution. Color code in the bias plots indicates the total observed precipitation in each time step. All downscaled model runs show an amplified diurnal cycle, though using explicit rather than parametrized convection appears to moderate this effect.

Simulations in progress: We use the WRF with the ARW core, version 4.3.1. The simulation domain is centered at 38.4°N and 98°W and has dimensions of 2050 (west-east) × 1750 (south-north) × 61 (vertical) grid points with grid spacing of 4 km, covering most North America including Alaska, Canada as well as Puerto Rico. A large ensemble simulation will be conducted using reanalysis as well as GCMs from CMIP6. The simulation will include: (1) 20 years (2000-2019) of simulation forced by reanalysis data ERA5; (2) 20 years of historical and future simulations for mid and end of 21st century, respectively using three GCMs from CMIP6 to cover the range of uncertainty of all the CMIP models to CO_2 doubling. Uncertainty due to internal variability and physics sensitivity will be also assessed as we did for the 12km simulations. We expect this dataset to improve on the Wang and Kotamarthi (2014) and Zobel et al. (2017) downscaled dataset.

References:

Chang, W., M. Stein, J. Wang, V. R. Kotamarthi, and E. Moyer, 2016: Changes in Spatio-temporal Precipitation Patterns in Changing Climate Conditions. Journal of Climate.29, 8355-8376. DOI: 10.1175/JCLI-D-15-0844.1.

Chang, W., J. Wang, J. Marohnic, V. R. Kotamarthi, and E.J. Moyer, 2018: Diagnosing added value of convection-permitting regional models using precipitation event identification and tracking. Climate Dynamics. https://doi.org/10.1007/s00382-018-4294-0.

Chen Chen, Won Chang, Jiali Wang, V. Rao Kotamarthi, Wenwen Kong, Michael L. Stein, Elisabeth J. Moyer. Convective precipitation events intensify but contract under global warming. Nature Climate Change. 2020. In review

Hong, S. Y., and J. J. Lim (2006), The WRF single-moment 6-class microphysics scheme (WSM6), J. Korean Meteor. Soc.,42, 129–151.

Grell, G. A., and D. Devenyi (2002), A generalized approach to parameterizing convection combining ensemble and data assimilation techniques, Geophys. Res. Lett.,29(14), 1693, doi:10.1029/2002GL015311.

Kain, J. S. (2004), The Kain–Fritsch convective parameterization: An update,J. Appl. Meteorol.,43, 170–181.

Wang, J., and V. R. Kotamarthi, 2014: Downscaling with a nested regional climate model in near-surface fields over the contiguous United States, Journal of Geophysical Research, Atmosphere, 119, 8778–8797.

Zobel, Z., J. Wang, D. J. Wuebbles, and V. R. Kotamarthi. 2017. Evaluations of high-resolution dynamically downscaled ensembles over the contiguous United States. Climate Dynamics. doi:10.1007/s00382-017-3645-6

NOAA's National Air Quality Forecast Capability for Ozone and Fine Particulate Matter

Jeffery McQueen[1], Pius Lee[2], Ivanka Stajner[1], Jianping Huang[3], Ho-Chun Huang[3] and Li Pan[3]

[1]NWS/NCEP/EMC – College Park, MD, [2]NOAA/OAR/ARL–College Park, MD, [3]IMSG–College Park, MD
Email: Jeff.McQueen@noaa.gov

The operational NOAA National Air Quality Forecast Capability, NAQFC, provides two day model forecasts of ozone and fine particulate matter surface concentrations twice per day at the 06 and 12 UTC cycles. The NAQFC operational forecast for ozone (O3) for the nation was implemented in September 2007 and for fine particulate matter (PM2.5) in January 2015 (Lee, et al., 2018). The NAQFC is made up of the North American Non-Hydrostatic Multiscale Model (NAM-NMMB) 12 km numerical weather prediction model and the EPA Community Model for Air Quality (CMAQ), using Carbon Bond-V (CB-V) gas phase chemistry and AERO-VI particulate matter processing. Predictions are available in real-time for the continental U.S., Alaska and Hawaii. Offline coupling between the NAM and CMAQ is achieved at hourly intervals by interpolation from the NAM to the CMAQ horizontal and vertical grids. Anthropogenic emissions are updated monthly from the EPA National Emission Inventory for the base year 2014V2. Wild fire smoke emissions were included in 2015 and are based on the U.S. Forest Service BlueSky smoke emission system and the NESDIS Hazardous Mapping System (HMS) fire locations, which are updated daily. Dust emissions were also updated with the NOAA/ARL Fengsha land use based dust emissions system (Dong, 2016). Dust lateral boundary conditions are provided by the NCEP NEMS Global Aerosol Capability (NGAC) V2 with climatological values from NASA GEOS-Chem for other species (Lu, et al., 2016; Wang, et al., 2018). In December 2018, the 12km L35 NAM-CMAQ V5.0.2 model analog ensemble bias correction was extended for both ozone and PM2.5 with improvements to adjust rare events (Huang, et al., 2018). Emissions for oil and gas sector activities were also updated. Predictions are available to U.S. state air quality forecasters and the public from the NWS National Digital Guidance Database (NDGD): http://airquality.weather.gov/ with experimental model predictions at http://www.emc.ncep.noaa.gov/mmb/aq/.

In 2019, Tests with a Unified Forecast System (UFS) based on the Global Forecast System (GFS) with a finite volume on cubed-sphere dynamic core continued with forecasts extended to 72 hours. Monthly average PM2.5 errors for August 2019 (Fig. 1) over CONUS show improvements with the experimental GFS-CMAQ model configuration. Smoke emissions from the NOAA/NESDIS Global Biomass Burning Emissions Product (GBBEPx) with fire radiative power (for plume rise) are included here as well as the provision of full aerosol lateral boundary conditions from the GEFS-Aerosol global model. GEFS-Aerosol is based on the GFS dynamic core inline aerosol global model at ~ 25 km out to 5 days with an expected implementation in the fall of 2020. The experimental GFS-CMAQ is expected to be implemented with upgrades to CMAQ version V5.3 with CB-VI gas phase and AERO-7 aerosol processes. These changes to NAQFC along with updates to anthropogenic emissions are also expected to be implemented in 2022.

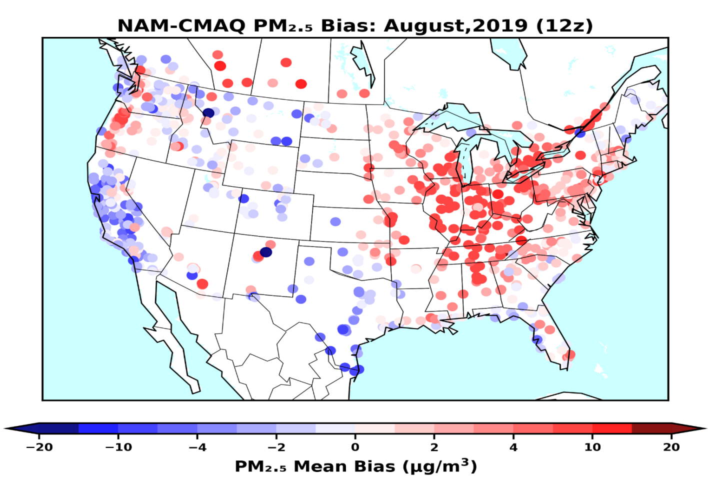

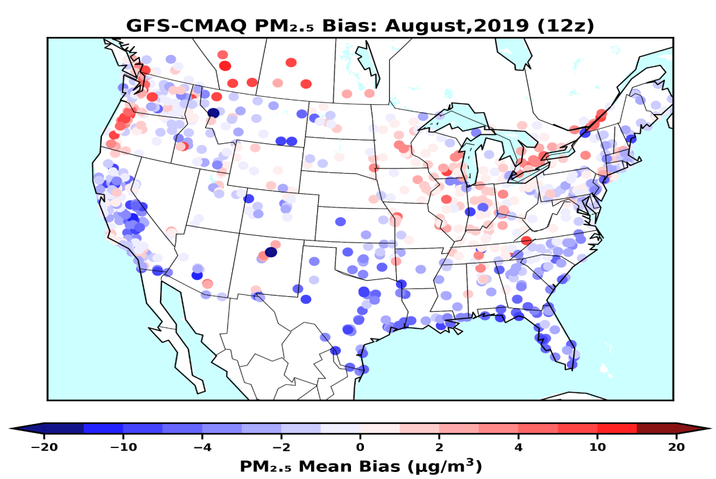

Figure 1. Comparison of Operational NAM-CMAQ day 1 24h avg PM2.5 model prediction bias vs experimental GFS-CMAQ averaged for all days during August 2019.

References

Huang, J., J. McQueen, J. Wilczak, I. Djalalova, I. Stajner, P. Shafran, D. Allured, P. Lee, L. Pan, D. Tong,H.-C. Huang, G. DiMego, S. Upadhayay, L. Delle Monache.(2017) Improving NOAA NAQFC PM2.5 predictions with a bias correction approach. Wea. Forec., 32,2. DOI: http://dx.doi.org/10.1175/WAF-D-16-0118.1

Lee, P., and Coauthors, 2017: NAQFC developmental forecast guidance for fine particulate matter PM2.5). Wea. Forecasting, doi:https://doi.org/10.1175/WAF-D-15-0163.1.

Lu, C.-H., A. da Silva, J. Wang, S. Moorthi, M. Chin, P. Colarco, Y. Tang, P. S. Bhattacharjee, S.-P.

Chen, H.-Y. Chuang, H-M. H. Juang, J. McQueen, and M. Iredell, 2016: The implementation of NEMSGFS Aerosol Component (NGAC) Version 1.0 for global dust forecasting at NOAA/NCEP, Geosci.Model Dev. Discuss., 9, 1-37.

Wang, J., Bhattacharjee, P. S., Tallapragada, V., Lu, C.-H., Kondragunta, S., da Silva, A., Zhang, X.,Chen, S.-P., Wei, S.-W., Darmenov, A. S., McQueen, J., Lee, P., Koner, P., and Harris, A.: The implementation of NEMS GFS Aerosol Component (NGAC) Version 2.0 for global multispecies forecasting at NOAA/NCEP – Part 1: Model descriptions. Geosci. Model Dev., 11, 2315–2332, 2018 https://doi.org/10.5194/gmd-11-2315-2018